

Measurement of the ${}^6\text{Li}(e,e'p)$ reaction cross sections at low momentum transfer

T. Hotta ^{a,1}, T. Tamae ^a, T. Miura ^a, H. Miyase ^b, I. Nakagawa ^a,
T. Suda ^b, M. Sugawara ^a, T. Tadokoro ^a, A. Takahashi ^a,
E. Tanaka ^a, H. Tsubota ^b

^aLaboratory of Nuclear Science, Tohoku University, Mikamine, Taihaku, Sendai,
Miyagi 982-0826, Japan

^bPhysics Department, Graduate School of Science, Tohoku University, Aramaki,
Aoba, Sendai, Miyagi 980-8578, Japan

Abstract

The triple differential cross sections for the ${}^6\text{Li}(e,e'p)$ reaction have been measured in the excitation energy range from 27 to 46 MeV in a search for evidence of the giant dipole resonance (GDR) in ${}^6\text{Li}$. The cross sections have no distinct structures in this energy region, and decrease smoothly with the energy transfer. Angular distributions are different from those expected with the GDR. Protons are emitted strongly in the momentum-transfer direction. The data are well reproduced by a DWIA calculation assuming a direct proton knockout process.

Key words: NUCLEAR REACTIONS: ${}^6\text{Li}(e,e'p)$; $E = 27\text{--}46$ MeV; measured $\sigma(E, \theta_e, \theta_p)$, missing energy spectra; deduced direct proton knockout process, DWIA analysis.

PACS: 24.30.Cz, 24.50.+g, 25.30.Rw, 27.20.+n

1 Introduction

The energy and width of the giant dipole resonance (GDR) smoothly vary with the atomic number in medium and heavy nuclei [1], while in light nuclei,

¹ Corresponding author. Present address: Research Center for Nuclear Physics, Osaka University, 10-1 Mihogaoka, Ibaraki, Osaka, 567-0047, Japan. e-mail: hotta@rcnp.osaka-u.ac.jp

the GDR is characterized by specific features for each nucleus [2]. For 1p-shell nuclei, some theoretical studies predict that the presence of the cluster structure causes supermultiplet splitting of the GDR [2]. For ${}^6\text{Li}$, Kurdyumov *et al.* [3] predicted by a translation invariant shell model calculation that the GDR splits into three multiplets with excitation energies of 10–12 MeV, 16–25 MeV and 31–35 MeV. According to their calculation, the state with the lowest excitation energy decays by proton or neutron emission leaving the residual nuclei, ${}^5\text{He}$ or ${}^5\text{Li}$, at the lowest $3/2^-$ and $1/2^-$ states. The state at 16–25 MeV decays through ${}^3\text{H}$ emission in addition to the one-nucleon decay to the lowest states of the residual nuclei. The state at 31–35 MeV predominantly decays into the $3/2^+$ state of the residual nuclei by emitting a proton or a neutron, whereas the decay into the lowest $3/2^-$ and $1/2^-$ states is forbidden because of spatial symmetry [3,4].

The experimental situation, however, is still unsettled. Using the yield-curve method, Denisov *et al.* [5] measured the photoproduction cross sections of charged particles for ${}^6\text{Li}$ in the photon energy E_γ region up to 55 MeV, and obtained the total photodisintegration cross section. Although the cross section was obtained from rather small number of data points, they claimed that three distinct peaks with a width about 5 MeV at about 11 MeV, 21 MeV and 30 MeV were observed. This result was consistent with the theoretical prediction. However, no later experiment has confirmed the presence of the GDR in ${}^6\text{Li}$ with such structures up to 30 MeV [6–8].

In order to discuss the presence of the GDR excitation and its decay properties in ${}^6\text{Li}$, we have measured the ${}^6\text{Li}(e,e'p)$ reaction cross sections for specific final states in the energy transfer region $\omega = 27\text{--}46$ MeV, covering a sufficiently high-energy region where the highest component of the GDR is predicted. In the case of $(e,e'p)$ reaction on heavier nuclei such as ${}^{12}\text{C}$ and ${}^{40}\text{Ca}$ [9,10], the GDR states are clearly observed as peaks in the cross sections at the same resonance energies observed in the photoreactions. The angular distributions for decay protons have the dipole characteristics, i.e. protons are strongly emitted to both the parallel and anti-parallel directions to the momentum transfer (\vec{q}).

In the high ω and $|\vec{q}|$ region, where the contribution from the giant resonances is small, the $(e,e'p)$ reactions are well understood as the direct knockout process, and a distorted wave impulse approximation (DWIA) gives a good description of the reaction [11]. In this case, protons are strongly emitted to the momentum transfer direction reflecting the momentum distribution of the proton in the ground state of the target nuclei.

It is expected that the contributions of the different reaction processes are identified by the angular distribution and its ω and $|\vec{q}|$ dependence. Therefore, we have measured the angular distribution of emitted protons at two different

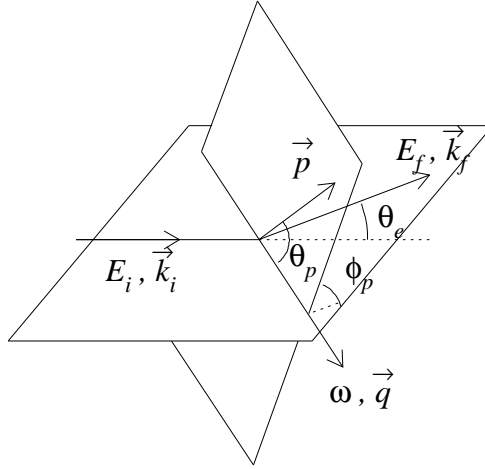


Fig. 1. Definition of the polar angle θ_p and azimuthal angle ϕ_p of proton momentum \vec{p} with respect to the momentum transfer \vec{q} . The incident- and scattered-electron momenta are represented by \vec{k}_i and \vec{k}_f .

electron scattering angles: (1) $\theta_e = 26^\circ$ where the momentum transfer $|\vec{q}|$ is 60–67 MeV/c, and (2) $\theta_e = 42^\circ$ where $|\vec{q}|=90$ MeV/c.

2 Experimental Setup

Figure 1 shows the kinematics of the (e,e'p) reaction and the definition of reaction angles. Energies of incident and scattered electrons are E_i and E_f , and θ_e denotes the scattered electron angle. The incident and scattered electrons define the scattering plane. An energy $\omega = E_i - E_f$ and a momentum $\vec{q} = \vec{k}_i - \vec{k}_f$ are transferred to the target nuclei. The direction of an emitted proton is defined by a polar angle θ_p and an azimuthal angle ϕ_p relative to the momentum transfer vector \vec{q} .

The experiment was carried out by using a 134 MeV continuous electron beam from the pulse stretcher ring, SSTR [12] at the Laboratory of Nuclear Science, Tohoku University. The beam intensity was in the range of 150–300 nA. The experimental setup is described in detail in a previous paper [13].

We used a 95% enriched, 6 mg/cm²-thick ⁶Li target. Oxygen contamination in the target was estimated from the elastic peak to be less than 0.1%. Scattered electrons were momentum-analyzed in a double-focusing magnetic spectrometer [14] having a solid angle of 2.9 msr, and detected in two layers of plastic scintillators and a vertical drift chamber (VDC) located in the focal plane. A typical momentum resolution was about 0.2% at 100 MeV/c. The electron spectrometer was set at $\theta_e = 26^\circ$ for $27 \text{ MeV} \leq \omega \leq 46 \text{ MeV}$, and at $\theta_e = 42^\circ$

for $34 \text{ MeV} \leq \omega \leq 39 \text{ MeV}$.

Protons were measured with detector telescopes, each consisting of one $50 \mu\text{m}$ -thick and 2 or 3 layers of 1 mm or 2 mm-thick silicon surface barrier detectors (SSD) with a sensitive area of 300 mm^2 . These telescopes were located at 12–18 cm from the target in every 30° step. They covered the angular range $0^\circ \leq \theta_p \leq 180^\circ$ for two planes having $\phi_p = -45^\circ$ and -135° . In order to reduce background, the detectors were shielded by lead. A pair of permanent magnets in front of each telescope removed low energy electrons emitted from the target. The acceptance solid angle of the telescope was defined by an iron collimator 2 mm in thickness, with an opening of 15 mm in diameter. The number of incident electrons was assessed by using a secondary emission monitor placed downstream of the target.

3 Data Reconstruction

Charged particles reaching at least the second layer of the SSD stack were used for the analysis. Particles stopped in the second layer were identified by plotting the energy deposited in the first layer (ΔE) against the energy deposited in the second layer (E), as shown in Fig. 2(a). Protons were distinguished from heavier particles such as deuterons and tritons using a particle-identification function defined by

$$f_{\text{PI}}(E) = \frac{\Delta E - \varepsilon_p(E)}{\varepsilon_t(E) - \varepsilon_p(E)}, \quad (1)$$

where $\varepsilon_p(E)$ and $\varepsilon_t(E)$ are the calculated energy deposits at the first layer for a proton and a triton having the energy deposit E at the second layer. The cut point of f_{PI} is shown as a curve in Fig. 2(a). Under this cut condition, typically 99% of protons stopping in the second layer was accepted and a typical background rate due to misidentified deuterons was 3%, slightly depending on the detector angle and the kinematical conditions. As seen in Fig. 2(a), particles with a small energy deposit in the first and second layer were clearly removed as background events due to electrons. Background electrons which reached the third layer were excluded from the plots due to their smaller energy deposit in the first and second layers. Particles which reached the third layer are dominated by protons. In this case, a proton was clearly identified by using energies deposited in the second and third layer (Fig. 2(b)).

The kinetic energy of emitted charged particles from the target was determined by summing the energy deposited in the stack of SSD layers. For particles which did not stop in the stack, the kinetic energy was estimated from the dE/dx measurements, assuming such particles to be protons. The recoil energy

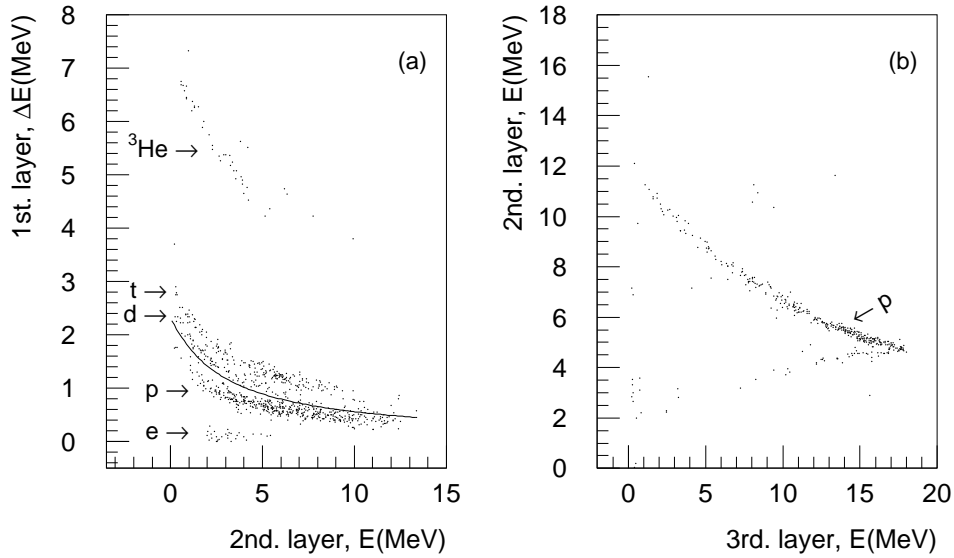


Fig. 2. Pulse height distributions for two layers of the SSD stack for particles stopping in (a) the second layer, and (b) in the third layer.

E_R of the residual system was deduced from the measured momenta of the electron and proton. Then the missing-energy E_m is calculated as

$$E_m = \omega - E_p - E_R, \quad (2)$$

where E_p is the kinetic energy of the emitted proton. The final state of the reaction is defined by this E_m . A triple differential cross sections $d^3\sigma/d\omega d\Omega_e d\Omega_p$ corresponding to specific final states were obtained by integrating proton yield over a certain range of E_m . The normalization of the cross section was made from elastic scattering by comparing the data with that of reference [15].

In general, the $(e, e'p)$ reaction cross section is decomposed into four terms [16];

$$\frac{d^3\sigma}{d\omega d\Omega_e d\Omega_p} = \sigma_L + \sigma_T + \sigma_{LT} \cos \phi_p + \sigma_{TT} \cos 2\phi_p, \quad (3)$$

where σ_L and σ_T are longitudinal and transverse terms, and the σ_{LT} and σ_{TT} are longitudinal-transverse and transverse-transverse interference terms, respectively. In the present experiment, protons were measured at $\phi_p = -45^\circ, -135^\circ$. Therefore, the $\sigma_{TT} \cos 2\phi_p$ term is always zero. The $\sigma_{LT} \cos \phi_p$ term contributes with opposite signs to the the cross sections at $\phi_p = -45^\circ$ and -135° , and

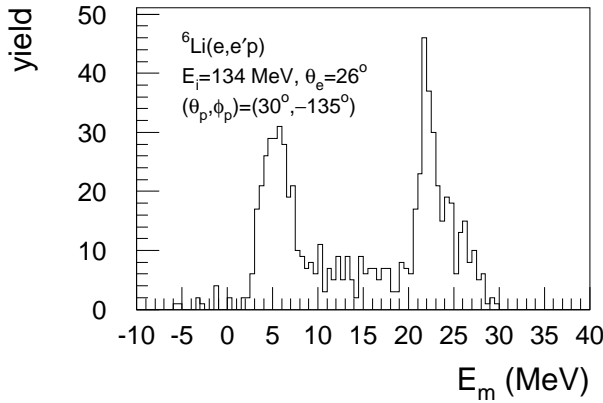


Fig. 3. Missing-energy spectrum for ${}^6\text{Li}(e,e'p)$ reaction.

does not contribute to a total cross section. In the analysis, the data were fitted with a linear combination of Legendre polynomials

$$\frac{d^3\sigma}{d\omega d\Omega_e d\Omega_p} = A_0 \left(1 + \sum_{i=1}^m a_i P_i(\cos \theta_p) + \cos \phi_p \sum_{j=1}^n b_j P_j^1(\cos \theta_p) \right). \quad (4)$$

The first and second terms in the equation (4) correspond to $\sigma_L + \sigma_T$ terms, and the third term corresponds to the $\sigma_{LT} \cos \phi_p$ term [16]. A least χ^2 fitting was carried out under the constraint that a triple differential cross section is not negative. The maximum order of fitting polynomials m and n were terminated when the χ^2 per the number of degrees of freedom (χ^2/NDF) did not decrease with a larger value of m or n .

By integrating a triple differential cross section $d^3\sigma/d\omega d\Omega_e d\Omega_p$ over proton emission angles, the double differential cross section $d^2\sigma/d\omega d\Omega_e$ was obtained as

$$\frac{d^2\sigma}{d\omega d\Omega_e} = 4\pi A_0. \quad (5)$$

4 Results and Discussions

Figure 3 shows an example of a missing-energy spectrum. Considering the level structure of ${}^5\text{He}$ [17], the peak at $E_m = 4.6$ MeV corresponds to the two-body breakup into proton and ${}^5\text{He}$ (g.s., $J^\pi = 3/2^-$). A ${}^5\text{He}$ nuclei is an

unstable nuclei, which has a ground state as a resonance with $\Gamma = 600$ keV at 0.89 MeV above the $\alpha + n$ threshold. The peak at $E_m = 21.4$ MeV corresponds to an excited state of ${}^5\text{He}$ with $J^\pi = 3/2^+$ at 60 keV above the $d + t$ threshold with a width of 60 keV. Events of three body breakup reaction, ${}^6\text{Li} \rightarrow \alpha + n + p$ appear in the E_m region from 4.6 to 21.4 MeV. In the region of $E_m \geq 21$ MeV, ${}^6\text{Li} \rightarrow p + d + t$ process contribute to the reaction. The reaction cross sections were obtained by integrating $(e, e'p)$ yields over the following three E_m regions.

Region-1: $2 < E_m \leq 8$ MeV,

Region-2: $8 < E_m \leq 20$ MeV,

Region-3: $20 < E_m \leq 23$ MeV.

For each E_m region, the measured triple differential cross sections for the ${}^6\text{Li}(e, e'p)$ reaction are listed in Tables 1, 2 and 3.

By using Eq. (5), the double differential ${}^6\text{Li}(e, e'p)$ cross sections were obtained from fitting of the triple differential cross sections with a function (4). The results of the fitting are listed in Table 4. For every E_m region, the double differential ${}^6\text{Li}(e, e'p)$ cross sections smoothly decrease with ω , as shown in Fig. 4.

In Fig. 4(c), data points for $\omega < 30$ MeV do not exist since integration of the triple differential cross section over θ_p was not possible because of the detection threshold for protons. However, cross sections at forward angles which are listed in the Table 3, also show a smooth ω dependence for $\omega < 30$ MeV. No distinct structure of the GDR is observed. Such smooth ω dependence is similar to the photoreaction cross section for $E_\gamma < 30$ MeV measured with monochromatic photons [6–8], and contrasts with the $(e, e'p)$ reactions for heavier nuclei [9,10] in the GDR energy regions, where an ω dependence of the peak of the GDR was observed. A theoretical prediction of the GDR states which decay into the $3/2^+$ state of ${}^5\text{He}$ at $E_m = 21$ MeV is shown in Fig. 4(d).

The angular distributions for each E_m regions are shown in Figs. 5, 6, and 7. Results of the fitting with function (4) are displayed by dashed curves.

Table 1

The triple differential ${}^6\text{Li}(e,e'p)$ cross section for E_m region-1 ($2 < E_m \leq 8$ MeV), in units of nb/MeV sr². Cross sections displayed with “<” sign are Poisson upper limits at a 68% confidence level, where no event was observed.

		θ_e and ω (MeV)										
		26°	26°	26°	26°	26°	26°	26°	26°	26°	42°	42°
(θ_p, ϕ_p)		27.2–28.4	28.4–29.5	29.5–30.6	30.6–31.8	31.8–32.9	31.7–35.0	35.0–37.2	36.6–41.5	41.7–46.6	34.0–36.6	36.6–39.1
$(0^\circ, -)$		15.9 ± 2.1	17.0 ± 2.2	12.0 ± 1.8	12.5 ± 1.7	8.3 ± 1.5	9.2 ± 0.8	7.2 ± 0.8	3.2 ± 0.4	1.5 ± 0.3	4.6 ± 0.6	3.5 ± 0.5
$(15^\circ, -135^\circ)$		–	–	–	–	–	9.5 ± 1.1	7.3 ± 1.2	–	–	–	–
$(30^\circ, -135^\circ)$		15.2 ± 2.1	13.5 ± 2.1	13.2 ± 2.1	9.0 ± 1.6	8.0 ± 1.5	8.2 ± 0.8	7.8 ± 1.0	0.5 ± 0.2	1.0 ± 0.3	2.1 ± 0.5	1.8 ± 0.5
$(45^\circ, -135^\circ)$		–	–	–	–	–	5.3 ± 0.8	4.2 ± 0.9	–	–	–	–
$(60^\circ, -135^\circ)$	∞	9.1 ± 1.7	4.7 ± 1.3	6.7 ± 1.5	3.2 ± 1.0	4.2 ± 1.1	2.2 ± 0.4	1.2 ± 0.4	0.6 ± 0.2	0.6 ± 0.2	0.7 ± 0.3	0.5 ± 0.3
$(75^\circ, -135^\circ)$		–	–	–	–	–	1.3 ± 0.5	1.0 ± 0.5	–	–	–	–
$(90^\circ, -135^\circ)$		1.1 ± 0.6	1.5 ± 0.7	1.1 ± 0.6	0.7 ± 0.4	0.5 ± 0.4	0.8 ± 0.3	0.6 ± 0.3	0.4 ± 0.2	–	0.2 ± 0.2	< 0.32
$(120^\circ, -135^\circ)$		0.2 ± 0.2	0.2 ± 0.2	< 0.39	< 0.33	0.2 ± 0.2	0.3 ± 0.3	0.4 ± 0.3	0.4 ± 0.2	–	< 0.33	< 0.35
$(150^\circ, -135^\circ)$		–	–	–	–	–	0.2 ± 0.2	0.6 ± 0.4	0.1 ± 0.1	–	0.2 ± 0.2	< 0.32
$(180^\circ, -)$		0.2 ± 0.2	0.2 ± 0.2	1.0 ± 0.4	< 0.30	0.18 ± 0.18	0.1 ± 0.1	< 0.31	0.4 ± 0.1	–	0.1 ± 0.1	< 0.24
$(30^\circ, -45^\circ)$		5.3 ± 1.2	5.8 ± 1.3	1.2 ± 0.6	4.7 ± 1.1	3.8 ± 1.0	2.2 ± 0.5	1.8 ± 0.5	1.0 ± 0.3	0.1 ± 0.1	0.1 ± 0.1	0.5 ± 0.3
$(45^\circ, -45^\circ)$		–	–	–	–	–	0.9 ± 0.4	0.7 ± 0.5	–	–	–	–
$(60^\circ, -45^\circ)$		1.0 ± 0.6	2.0 ± 0.8	1.7 ± 0.8	1.2 ± 0.6	1.2 ± 0.6	0.8 ± 0.4	0.5 ± 0.3	0.5 ± 0.2	0.2 ± 0.1	0.3 ± 0.2	0.2 ± 0.2
$(75^\circ, -45^\circ)$		–	–	–	–	–	0.7 ± 0.4	< 0.63	–	–	–	–
$(90^\circ, -45^\circ)$		2.0 ± 0.7	1.9 ± 0.7	0.7 ± 0.4	1.2 ± 0.5	1.5 ± 0.6	1.7 ± 0.4	1.4 ± 0.4	0.4 ± 0.1	0.1 ± 0.1	0.4 ± 0.2	< 0.24
$(120^\circ, -45^\circ)$		1.6 ± 0.6	0.5 ± 0.3	1.3 ± 0.6	1.1 ± 0.5	0.2 ± 0.2	0.8 ± 0.3	0.1 ± 0.1	0.6 ± 0.2	–	< 0.29	0.3 ± 0.2
$(150^\circ, -45^\circ)$		–	–	–	–	–	0.6 ± 0.3	0.2 ± 0.2	0.1 ± 0.1	–	< 0.26	< 0.28

Table 2

Same as for Table 1, but for E_m region-2 ($8 < E_m \leq 20$ MeV).

(θ_p, ϕ_p)	θ_e and ω (MeV)										
	26°	26°	26°	26°	26°	26°	26°	26°	26°	42°	42°
$(0^\circ, -)$	27.2–28.4	28.4–29.5	29.5–30.6	30.6–31.8	31.8–32.9	31.7–35.0	35.0–37.2	36.6–41.5	41.7–46.6	34.0–36.6	36.6–39.1
$(0^\circ, -)$	10.7 ± 1.7	11.2 ± 1.8	12.0 ± 1.8	9.1 ± 1.4	7.3 ± 1.4	9.3 ± 0.8	7.2 ± 0.8	4.3 ± 0.4	2.6 ± 0.4	3.1 ± 0.5	2.8 ± 0.5
$(15^\circ, -135^\circ)$	–	–	–	–	–	6.7 ± 0.9	7.6 ± 1.2	–	–	–	–
$(30^\circ, -135^\circ)$	17.0 ± 2.3	12.6 ± 2.0	16.4 ± 2.3	10.4 ± 1.7	10.3 ± 1.7	7.3 ± 0.8	4.8 ± 0.8	3.3 ± 0.4	4.3 ± 0.6	2.2 ± 0.5	2.4 ± 0.6
$(45^\circ, -135^\circ)$	–	–	–	–	–	4.3 ± 0.8	4.8 ± 1.0	–	–	–	–
$(60^\circ, -135^\circ)$	5.2 ± 1.3	5.4 ± 1.4	4.4 ± 1.2	4.6 ± 1.1	7.5 ± 1.5	3.3 ± 0.5	2.3 ± 0.5	2.2 ± 0.3	1.4 ± 0.3	2.1 ± 0.6	0.9 ± 0.4
$(75^\circ, -135^\circ)$	–	–	–	–	–	2.7 ± 0.7	1.5 ± 0.6	–	–	–	–
$(90^\circ, -135^\circ)$	1.7 ± 0.7	1.2 ± 0.6	1.7 ± 0.7	0.9 ± 0.5	1.0 ± 0.5	1.0 ± 0.3	0.5 ± 0.3	1.6 ± 0.4	–	0.3 ± 0.2	0.4 ± 0.2
$(120^\circ, -135^\circ)$	1.3 ± 0.5	1.6 ± 0.6	0.6 ± 0.4	1.1 ± 0.4	0.2 ± 0.2	1.3 ± 0.4	0.7 ± 0.3	0.4 ± 0.2	–	0.2 ± 0.2	0.4 ± 0.3
$(150^\circ, -135^\circ)$	–	–	–	–	–	0.6 ± 0.3	0.9 ± 0.5	0.5 ± 0.2	–	0.2 ± 0.2	0.2 ± 0.2
$(180^\circ, -)$	3.4 ± 0.8	1.7 ± 0.6	1.8 ± 0.6	1.5 ± 0.5	1.8 ± 0.6	0.5 ± 0.2	0.9 ± 0.3	0.7 ± 0.2	–	0.1 ± 0.1	< 0.24
$(30^\circ, -45^\circ)$	7.6 ± 1.5	6.1 ± 1.4	7.9 ± 1.6	5.7 ± 1.2	4.1 ± 1.0	3.6 ± 0.6	3.3 ± 0.7	1.1 ± 0.3	1.0 ± 0.3	1.4 ± 0.4	1.3 ± 0.4
$(45^\circ, -45^\circ)$	–	–	–	–	–	1.3 ± 0.5	2.0 ± 0.8	–	–	–	–
$(60^\circ, -45^\circ)$	4.2 ± 1.2	4.4 ± 1.2	4.1 ± 1.2	4.0 ± 1.1	2.4 ± 0.9	0.5 ± 0.3	0.8 ± 0.4	1.2 ± 0.3	0.9 ± 0.3	0.5 ± 0.3	0.8 ± 0.4
$(75^\circ, -45^\circ)$	–	–	–	–	–	2.2 ± 0.7	3.1 ± 1.0	–	–	–	–
$(90^\circ, -45^\circ)$	3.2 ± 0.8	4.5 ± 1.0	5.0 ± 1.1	0.8 ± 0.4	2.9 ± 0.8	2.0 ± 0.5	1.2 ± 0.5	1.2 ± 0.3	0.2 ± 0.1	0.5 ± 0.2	0.3 ± 0.2
$(120^\circ, -45^\circ)$	2.7 ± 0.8	3.8 ± 1.0	2.0 ± 0.7	3.4 ± 0.8	1.7 ± 0.6	1.0 ± 0.3	1.8 ± 0.4	1.0 ± 0.3	–	0.3 ± 0.2	< 0.31
$(150^\circ, -45^\circ)$	–	–	–	–	–	1.3 ± 0.4	2.6 ± 0.7	0.6 ± 0.2	–	1.0 ± 0.4	0.3 ± 0.2

Table 3

Same as for Table 1, but for E_m region-3 ($20 < E_m \leq 23$ MeV).

	θ_e and ω (MeV)										
	26°	26°	26°	26°	26°	26°	26°	26°	26°	26°	42°
(θ_p, ϕ_p)	27.2–28.4	28.4–29.5	29.5–30.6	30.6–31.8	31.8–32.9	31.7–35.0	35.0–37.2	36.6–41.5	41.7–46.6	34.0–36.6	36.6–39.1
$(0^\circ, -)$	8.8 ± 1.6	9.5 ± 1.7	9.0 ± 1.6	10.9 ± 1.6	6.6 ± 1.3	11.8 ± 0.9	10.7 ± 1.0	5.0 ± 0.5	3.0 ± 0.4	6.4 ± 0.7	6.5 ± 0.7
$(15^\circ, -135^\circ)$	–	–	–	–	–	8.0 ± 1.0	7.3 ± 1.2	–	–	–	–
$(30^\circ, -135^\circ)$	9.3 ± 1.7	9.3 ± 1.7	9.3 ± 1.7	11.8 ± 1.8	8.8 ± 1.6	9.3 ± 0.9	7.0 ± 0.9	3.6 ± 0.5	2.2 ± 0.4	2.1 ± 0.5	2.2 ± 0.5
$(45^\circ, -135^\circ)$	–	–	–	–	–	5.5 ± 0.9	5.4 ± 1.1	–	–	–	–
$(60^\circ, -135^\circ)$	–	3.0 ± 1.0	3.0 ± 1.0	2.3 ± 0.8	3.9 ± 1.1	1.8 ± 0.4	1.2 ± 0.4	1.9 ± 0.3	1.1 ± 0.3	0.9 ± 0.3	0.5 ± 0.3
$(75^\circ, -135^\circ)$	–	–	–	–	–	1.1 ± 0.4	0.5 ± 0.4	–	–	–	–
$(90^\circ, -135^\circ)$	–	0.6 ± 0.4	1.1 ± 0.6	< 0.42	1.0 ± 0.5	0.2 ± 0.2	0.5 ± 0.3	0.2 ± 0.1	–	< 0.30	0.2 ± 0.2
$(120^\circ, -135^\circ)$	–	–	0.4 ± 0.3	0.5 ± 0.3	0.4 ± 0.3	0.2 ± 0.3	< 0.51	0.5 ± 0.2	–	0.5 ± 0.3	< 0.35
$(150^\circ, -135^\circ)$	–	–	–	–	–	< 0.36	0.6 ± 0.4	0.4 ± 0.2	–	< 0.30	0.2 ± 0.2
$(180^\circ, -)$	–	–	0.8 ± 0.4	1.2 ± 0.4	0.9 ± 0.4	0.1 ± 0.1	0.6 ± 0.2	0.4 ± 0.1	–	< 0.22	0.1 ± 0.1
$(30^\circ, -45^\circ)$	2.3 ± 0.8	1.8 ± 0.7	4.6 ± 1.2	3.9 ± 1.0	3.2 ± 0.9	1.2 ± 0.4	2.1 ± 0.5	1.1 ± 0.3	0.4 ± 0.2	1.0 ± 0.4	0.8 ± 0.3
$(45^\circ, -45^\circ)$	–	–	–	–	–	1.5 ± 0.6	1.0 ± 0.6	–	–	–	–
$(60^\circ, -45^\circ)$	–	0.7 ± 0.5	1.7 ± 0.8	1.7 ± 0.7	1.5 ± 0.7	0.6 ± 0.3	0.4 ± 0.4	0.4 ± 0.2	0.7 ± 0.3	0.5 ± 0.3	0.2 ± 0.2
$(75^\circ, -45^\circ)$	–	–	–	–	–	1.1 ± 0.5	0.7 ± 0.5	–	–	–	–
$(90^\circ, -45^\circ)$	–	1.4 ± 0.6	2.8 ± 0.8	1.0 ± 0.4	2.1 ± 0.7	1.5 ± 0.4	0.8 ± 0.4	0.7 ± 0.2	0.2 ± 0.2	0.4 ± 0.2	0.4 ± 0.2
$(120^\circ, -45^\circ)$	–	–	1.6 ± 0.6	1.5 ± 0.5	1.3 ± 0.5	1.0 ± 0.3	0.7 ± 0.3	0.8 ± 0.3	–	0.5 ± 0.3	0.5 ± 0.3
$(150^\circ, -45^\circ)$	–	–	–	–	–	0.6 ± 0.3	0.8 ± 0.4	0.3 ± 0.1	–	0.1 ± 0.1	< 0.28

Table 4
Fitting parameters in the function (4).

θ_e	ω (MeV)	A_0 (nb MeV ⁻¹ sr ⁻¹)	a_1	a_2	a_3	a_4	b_1	b_2	b_3	b_4	χ^2/NDF
Region 1; $2 < E_m \leq 8$ MeV											
26°	27.2-28.4	3.5 ± 0.3	1.5 ± 0.1	1.1 ± 0.2	0.5 ± 0.1	—	0.4 ± 0.1	0.53 ± 0.07	0.30 ± 0.04	—	0.84
26°	28.4-29.5	2.9 ± 0.2	1.6 ± 0.1	1.1 ± 0.1	0.4 ± 0.1	—	0.2 ± 0.1	0.31 ± 0.07	0.18 ± 0.04	—	3.37
26°	29.5-30.6	2.5 ± 0.2	1.5 ± 0.2	1.0 ± 0.2	0.1 ± 0.1	—	0.45 ± 0.07	0.68 ± 0.07	0.36 ± 0.07	0.14 ± 0.04	3.98
26°	30.6-31.8	2.0 ± 0.2	1.7 ± 0.1	1.4 ± 0.1	1.1 ± 0.1	0.32 ± 0.09	0.12 ± 0.08	0.38 ± 0.07	0.17 ± 0.03	—	1.46
26°	31.8-32.9	1.8 ± 0.2	1.7 ± 0.2	1.1 ± 0.2	0.3 ± 0.1	—	0.2 ± 0.1	0.32 ± 0.09	0.27 ± 0.08	0.05 ± 0.04	0.95
26°	31.7-35.0	1.73 ± 0.08	1.30 ± 0.06	1.05 ± 0.09	1.10 ± 0.09	0.44 ± 0.09	0.26 ± 0.05	0.35 ± 0.04	0.30 ± 0.02	0.16 ± 0.02	1.23
26°	35.0-37.2	1.31 ± 0.08	1.37 ± 0.08	1.2 ± 0.1	1.2 ± 0.1	0.5 ± 0.1	0.42 ± 0.07	0.24 ± 0.05	0.35 ± 0.04	0.23 ± 0.03	2.31
26°	36.6-41.5	0.57 ± 0.05	0.9 ± 0.1	0.6 ± 0.2	1.0 ± 0.2	0.9 ± 0.2	0.05 ± 0.1	0.03 ± 0.06	-0.03 ± 0.06	—	5.02
42°	34.0-36.6	0.52 ± 0.07	1.6 ± 0.3	1.1 ± 0.3	0.3 ± 0.2	—	0.4 ± 0.1	0.4 ± 0.1	0.27 ± 0.08	—	6.56
42°	36.6-39.1	0.34 ± 0.05	2.0 ± 0.4	2.1 ± 0.3	1.6 ± 0.4	0.6 ± 0.2	0.1 ± 0.1	0.3 ± 0.1	0.13 ± 0.07	—	2.86
Region 2; $8 < E_m \leq 20$ MeV											
26°	27.2-28.4	4.3 ± 0.2	0.9 ± 0.1	0.9 ± 0.1	0.1 ± 0.1	—	0.02 ± 0.08	0.20 ± 0.07	0.15 ± 0.06	—	2.23
26°	28.4-29.5	4.2 ± 0.2	0.9 ± 0.1	0.5 ± 0.1	0.3 ± 0.1	—	-0.10 ± 0.08	0.19 ± 0.06	0.22 ± 0.07	—	0.24
26°	29.5-30.6	3.9 ± 0.3	1.2 ± 0.1	0.6 ± 0.1	0.3 ± 0.1	0.4 ± 0.2	-0.07 ± 0.08	0.15 ± 0.05	0.22 ± 0.05	—	2.83
26°	30.6-31.8	3.1 ± 0.2	0.9 ± 0.2	1.1 ± 0.1	0.2 ± 0.2	-0.5 ± 0.2	0.01 ± 0.08	0.25 ± 0.07	0.02 ± 0.06	—	1.53

Table 4—continued

θ_e	ω (MeV)	A_0 (nb MeV ⁻¹ sr ⁻¹)	a_1	a_2	a_3	a_4	b_1	b_2	b_3	b_4	χ^2/NDF
Region 2; $8 < E_m \leq 20$ MeV – continued.											
26°	31.8-32.9	3.0 ± 0.3	1.1 ± 0.1	0.6 ± 0.2	-0.1 ± 0.1	–	0.1 ± 0.1	0.33 ± 0.08	0.24 ± 0.07	–	0.40
26°	31.7-35.0	2.0 ± 0.1	1.09 ± 0.08	0.8 ± 0.1	0.8 ± 0.1	0.4 ± 0.1	-0.17 ± 0.07	0.27 ± 0.05	0.16 ± 0.04	–	2.42
26°	35.0-37.2	1.9 ± 0.1	0.8 ± 0.1	0.9 ± 0.1	0.6 ± 0.1	–	-0.12 ± 0.07	0.27 ± 0.06	0.10 ± 0.05	–	1.55
26°	36.6-41.5	1.32 ± 0.07	0.82 ± 0.08	0.2 ± 0.1	0.2 ± 0.1	0.4 ± 0.1	0.19 ± 0.06	0.32 ± 0.04	0.12 ± 0.03	–	2.82
42°	34.0-36.6	0.82 ± 0.09	1.1 ± 0.2	0.8 ± 0.2	0.4 ± 0.2	–	0.2 ± 0.1	0.4 ± 0.1	0.08 ± 0.07	–	1.54
42°	36.6-39.1	0.65 ± 0.06	1.4 ± 0.2	1.1 ± 0.2	0.6 ± 0.2	–	0.2 ± 0.1	0.0 ± 0.1	0.09 ± 0.07	0.1 ± 0.06	0.53
Region 3; $20 < E_m \leq 23$ MeV											
26°	29.5-30.6	2.3 ± 0.2	1.2 ± 0.1	0.7 ± 0.2	0.6 ± 0.2	0.4 ± 0.2	-0.01 ± 0.08	0.25 ± 0.08	0.24 ± 0.06	–	0.42
26°	30.6-31.8	2.2 ± 0.2	1.3 ± 0.1	1.6 ± 0.1	0.8 ± 0.1	–	0.06 ± 0.07	0.42 ± 0.07	0.19 ± 0.05	0.18 ± 0.03	1.28
26°	31.8-32.9	2.2 ± 0.2	1.1 ± 0.2	0.8 ± 0.2	0.2 ± 0.2	–	0.2 ± 0.1	0.31 ± 0.09	0.3 ± 0.1	–	0.46
26°	31.7-35.0	1.62 ± 0.09	1.41 ± 0.08	1.23 ± 0.08	1.06 ± 0.08	0.41 ± 0.05	0.20 ± 0.04	0.47 ± 0.04	0.40 ± 0.03	0.19 ± 0.02	5.06
26°	35.0-37.2	1.4 ± 0.1	1.4 ± 0.1	1.5 ± 0.1	1.2 ± 0.2	0.7 ± 0.2	0.21 ± 0.09	0.37 ± 0.06	0.30 ± 0.05	0.14 ± 0.05	2.46
26°	36.6-41.5	1.02 ± 0.06	1.05 ± 0.09	1.00 ± 0.08	0.6 ± 0.1	–	0.24 ± 0.07	0.39 ± 0.06	0.29 ± 0.04	–	2.98
42°	34.0-36.6	0.71 ± 0.06	1.3 ± 0.2	1.6 ± 0.2	1.3 ± 0.1	–	-0.01 ± 0.08	0.22 ± 0.09	0.11 ± 0.05	–	5.84
42°	36.6-39.1	0.58 ± 0.07	1.8 ± 0.2	1.8 ± 0.3	1.7 ± 0.3	1.0 ± 0.3	0.0 ± 0.1	0.3 ± 0.1	0.20 ± 0.07	–	4.86

Table 5

Parameters of harmonic oscillator wave functions used for the calculation.

	relative strength		
	1s	1p	b (fm)
$2 < E_m \leq 8$ MeV	0.3	0.25	2.03
$8 < E_m \leq 9.7$ MeV	0.18	0.13	2.03
$9.7 < E_m \leq 20$ MeV	0.19	0.0	1.5
$20 < E_m \leq 23$ MeV	0.35	0.03	2.03

For every final state, triple differential cross sections are large at small angles of θ_p , the proton angle with respect to the momentum transfer. This characteristic is observed over all the measured energy and momentum region. The angular distribution is different from that for heavier nuclei. In the cases of ^{12}C and ^{40}Ca , protons are strongly emitted to $\theta_p = 0^\circ$ and 180° , which indicates that the excitation of the dipole states dominate the reaction mechanism. The observed angular distribution with a peak at forward angles indicates that the dipole excitation is not a dominant process, and higher multipoles contribute to the reaction. In the present statistics and the number of data points, most of data are well fitted within the fourth order of Legendre polynomials. However, for the E_m region-1 and 3, cross sections at the forward angle excess the Legendre curves at higher energies and momentum transfers. Higher multipoles than the quadrupole may contribute to the reaction.

The cross sections decrease smoothly with ω and the angular distributions show a forward peak. It implies that the direct proton knockout process dominates the $^6\text{Li}(e,e'p)$ reaction. Therefore, we compared the measured triple differential cross section with a distorted wave impulse approximation (DWIA) calculation which assumes a direct transition of a proton from the bound states to continuum states with distortion due to the interaction with the residual nucleus [18]. Ingredients of the calculation are then the bound state wave function of a proton in ^6Li and the optical potential between the emitted proton and the residual nucleus. Although the ^6Li ground state wave function with a large shell-model space based on a microscopic cluster model [19] was used for a precise analysis of quasi-elastic $^6\text{Li}(e,e'p)$ data [11], we used a linear combination of harmonic oscillator wave functions for 1s and 1p states to simplify the calculation. The strengths of these states were adjusted to reproduce the $^6\text{Li}(e,e'p)$ cross sections in the quasi-elastic region [11]. Parameters of the wave functions used in the calculation are listed in Table 5. The size parameter of the harmonic oscillator $b = 2.03$ fm was taken from the value determined by elastic and inelastic electron scattering experiment on ^6Li [20]. Following the analysis of the quasi-elastic experiment [11], the E_m region-2 was decomposed into two parts in the calculation ($8 < E_m \leq 9.7$ MeV and $9.7 < E_m \leq 20$ MeV). In order to reproduce the quasi-elastic data for $9.7 < E_m \leq 20$ MeV, the b param-

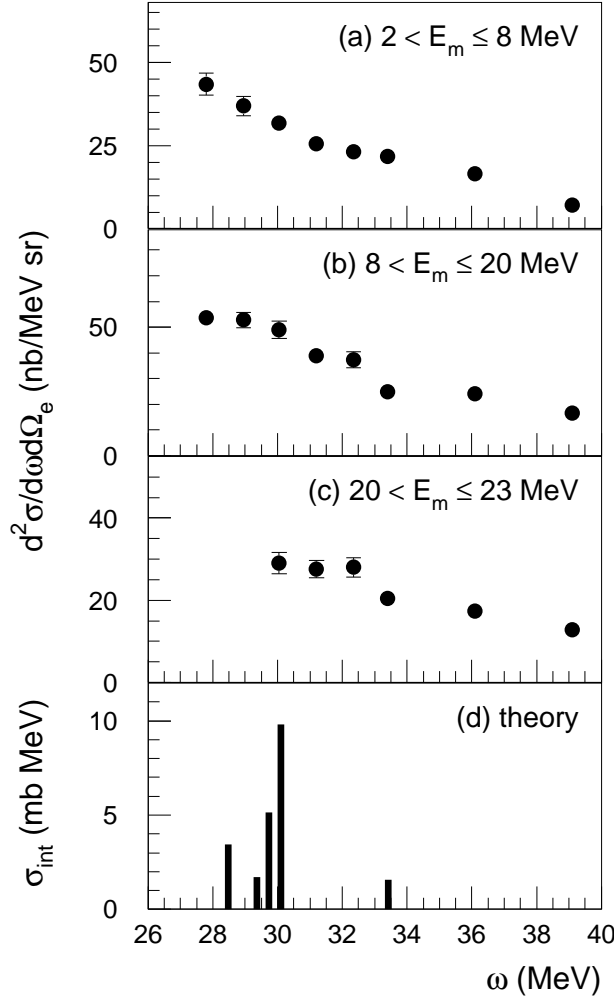


Fig. 4. The ${}^6\text{Li}(e,e'p)$ cross section at $\theta_e = 26^\circ$, integrated over proton emission angle. (a) for E_m region 1, (b) for 2, and (c) for 3. The calculated total photo absorption cross section from Ref. [3] is shown in (d).

eter was adjusted to 1.5 fm. Energy-dependent optical potential parameters were used in the calculation, which were determined from proton scattering in the energy range of 10–50 MeV for 1p-shell nuclei [21].

The results of the DWIA calculation are compared with the experimental cross section in Fig. 5–7. For every E_m region, the cross section obtained from the DWIA calculation exceeds the measured cross section. For the comparison, the DWIA results were multiplied by a common normalization factor obtained from the least χ^2 fitting of data for every E_m region and measured energy and momentum transfer region. A normalization factor 0.50 was found to give an overall agreement of the DWIA result with the experimental data of both

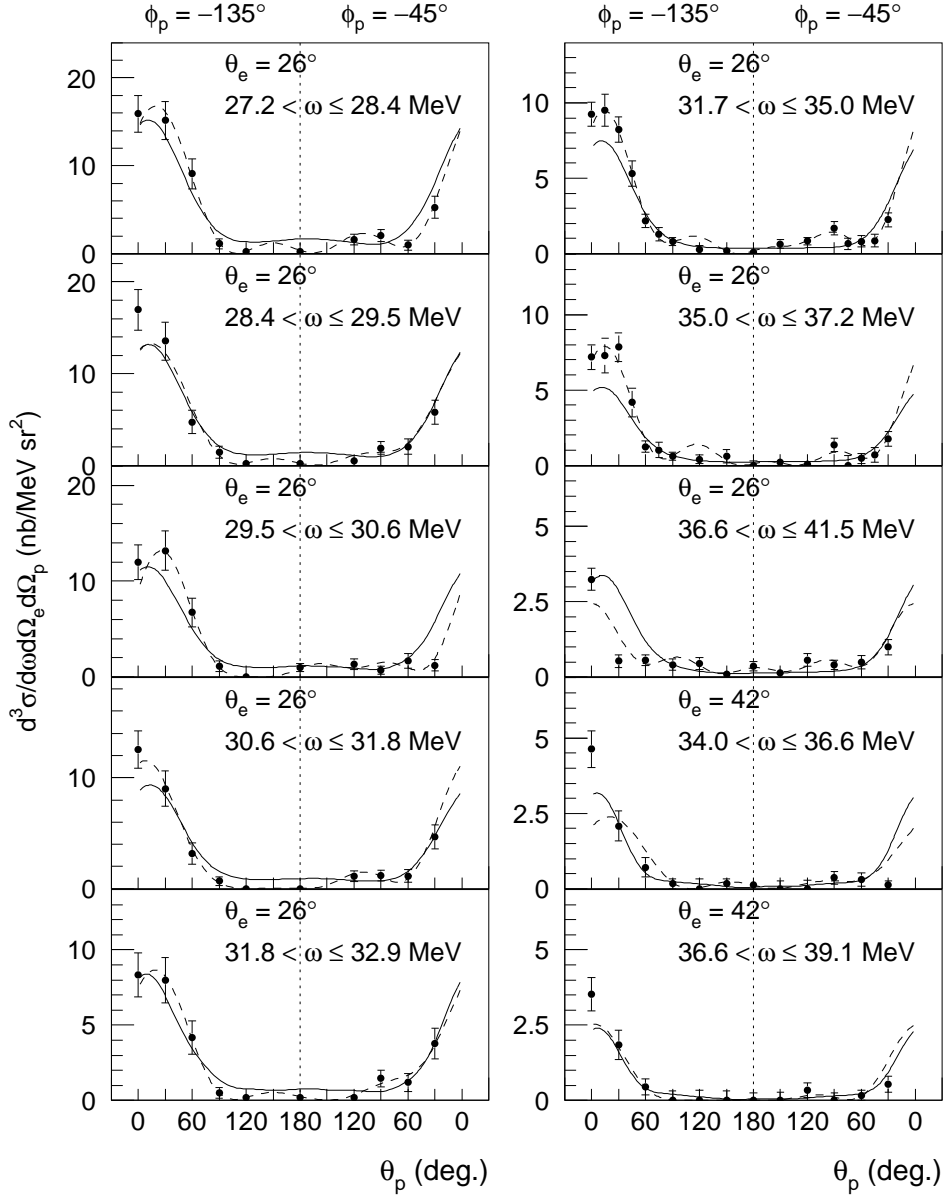


Fig. 5. Angular distributions of the triple differential cross sections for the ${}^6\text{Li}(e,e'p)$ reactions for E_m region-1 ($2 < E_m \leq 8$ MeV). Solid curves show the result of the DWIA calculation multiplied by 0.50. The dashed curves show the fitting with the Legendre polynomials.

the angular distribution and the ω dependence. Comparing with measured data of $|\vec{q}| = 90$ MeV/ c at $\theta_e = 42^\circ$ and 60–67 MeV/ c at $\theta_e = 26^\circ$, the DWIA calculation also reproduced the $|\vec{q}|$ -dependence of the cross section. For $\theta_p = 30^\circ$ and 60° , larger cross sections were observed for $\phi_p = -135^\circ$ than

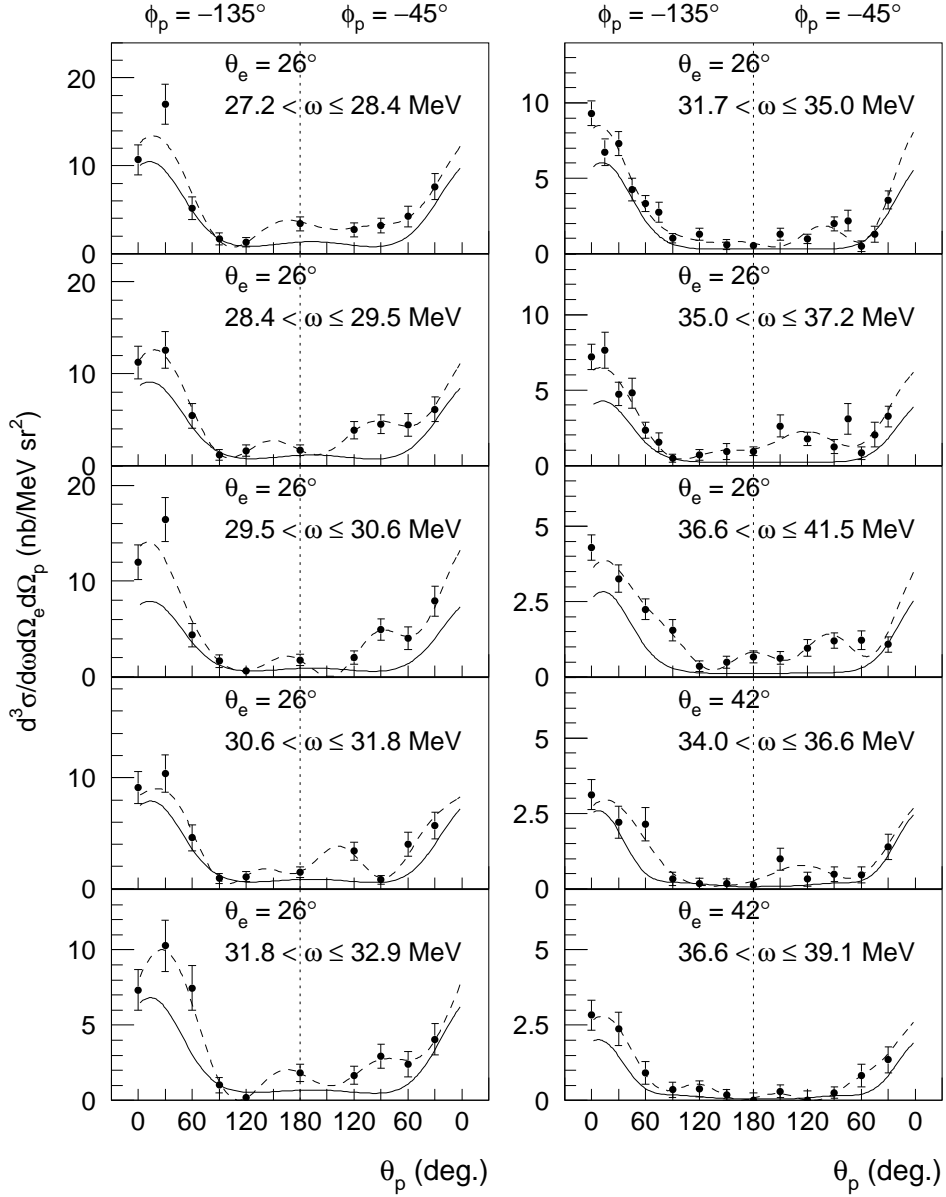


Fig. 6. Same as Fig. 5, but for E_m region-2 ($8 < E_m \leq 20$ MeV).

for $\phi_p = -45^\circ$ (Fig. 5–7). As explained in the previous section, this difference is due to the contribution of the longitudinal-transverse interference term, σ_{LT} . The DWIA calculation also reproduced the σ_{LT} contributions.

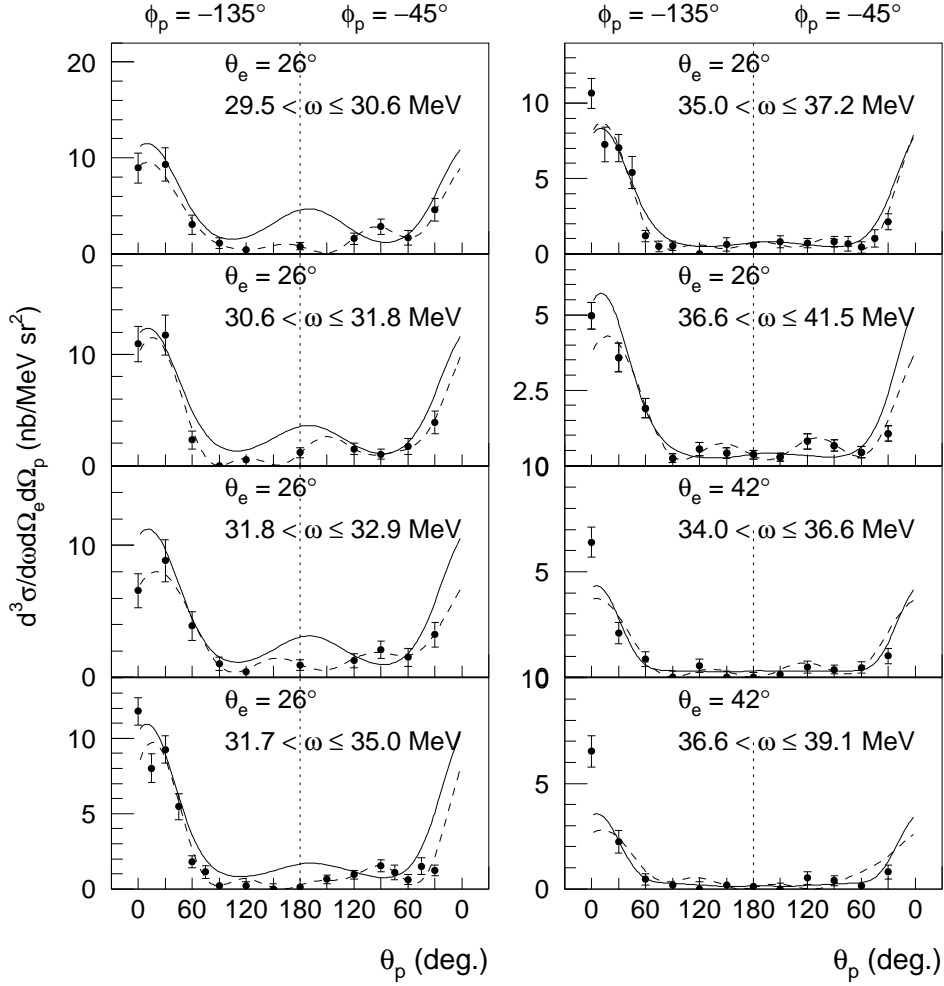


Fig. 7. Same as Fig. 5, but for E_m region-3 ($20 < E_m \leq 23$ MeV).

5 Conclusion

The ${}^6\text{Li}(e,e'p)$ reaction cross sections have been measured at ($\theta_e = 26^\circ$, $27.2 \leq \omega \leq 46.4$ MeV, $|\vec{q}|=60\text{--}67$ MeV) and ($\theta_e = 42^\circ$, $34.0 \leq \omega \leq 39.1$ MeV, $|\vec{q}|=90$ MeV), and were separated into three E_m regions corresponding to different final states: (1) residual ${}^5\text{He}$ in $3/2^-$ ground state, (2) three-body breakup into $\alpha+n+p$, and (3) residual ${}^5\text{He}$ in $3/2^+$, 16.7 MeV state. Although dipole states which decay into $3/2^+$ state were predicted around 30 MeV [3], the double differential cross section decreases smoothly with ω , and no distinct peak of the expected GDR is observed for every final state. This smooth ω -dependence is similar to photoreaction results for $E_\gamma < 30$ MeV except that of Denisov *et al.* [5]. Angular distributions of triple differential cross sections have

a peak at the direction of momentum transfer. This common characteristic is observed in the entire region of the measured energy and momentum transfer, in contrast with the results of other (e,e'p) reactions on ^{12}C and ^{40}Ca where the GDR is clearly observed. On the other hand, the DWIA calculation reproduces well the experimental data with only one normalization factor. This agreement indicates that the direct process dominates the $^6\text{Li}(e,e'p)$ reactions in this energy and momentum transfer region.

In order to study the (e,e'p) reaction mechanism more precisely, further calculations with a microscopic cluster model [19] for the ^6Li ground state wave function might be needed.

Acknowledgements

We express our thanks to the accelerator crew and staffs of the Laboratory of Nuclear Science, Tohoku University for their excellent operation of the accelerator and the experimental apparatus.

We would like to thank Prof. C. Giusti and Prof. G. van der Steenhoven for helping us to carry out the DWIA calculation with the computer code DWEEPY.

We would also like to thank Prof. G.A. Peterson for a careful reading of the manuscript.

References

- [1] J. Speth and A. van der Woude, Rep. Prog. Phys., **44** (1981) 720.
- [2] R.A. Eramzhyan, B.S. Ishkhanov, I.M. Kapitonov and V.G. Neudatchin, Phys. Rep. **136** (1986) 229.
- [3] I.V. Kurdyumov, S.H.El. Samarai, Yu.F. Smirnov and K.V. Shitikova, Izv. Akad. Nauk SSSR, Ser. Fiz. **30** (1966) 292.
I.V. Kurdyumov, Yu.F. Smirnov, K.V. Shitikova and S.Kh.El. Samarai, Phys. Lett. **B31** (1970) 163.
- [4] G.F. Filippov, V.S. Vasilevskii, S.P. Kruchinin and L.L. Chopovskii, Sov. Jou. Nucl. Phys. **43** (1986) 536.
- [5] V.P. Denisov, A.P. Komar, L.A. Kul'chitskii and E.D. Makhnovskii, Sov. Jou. Nucl. Phys. **5** (1967) 349.

- [6] G. Junghans, K. Bangert, U.E.P. Berg, R. Stock and K. Wienhard, *Z. Phys.* **A291** (1979) 353.
- [7] B.L. Berman and S.C. Fultz, *Rev. Mod. Phys.* **47** (1975) 713.
- [8] J. Ahrens, H. Borchert, K.H. Czock, H.B. Eppler, H. Gimm, H. Gundrum, M. Kröning, P. Riehn, G. Sitaram, A. Zieger and B. Ziegler, *Nucl. Phys.* **A251** (1975) 479.
- [9] J.R. Calarco, *Nucl. Phys.* **A569** (1994) 363c.
- [10] P. von Neumann-Cosel, H. Diesener, U. Helm, G. Herbert, V. Huck, A. Richter, G. Schrieder, A. Stascheck, A. Stiller, J. Ryckebusch, J. Carter, A.A. Cowley, R.W. Fearick, J.J. Lawrie, S.J. Mills, R.T. Newman, J.V. Pilcher, F.D. Smit, Z.Z. Vilakazi and D.M. Whittal, *Nucl. Phys.* **A569** (1994) 373c.
- [11] J.B.J.M. Lanen, A.M. van den Berg, H.P. Blok, J.F.J. van den Brand, C.T. Christou, R. Ent, A.G.M. van Hees, E. Jans, G.J. Kramer, L. Lapikás, D.R. Lehman, W.C. Parke, E.N.M. Quint, G. van der Steenhoven and P.K.A. de Witt Huberts, *Phys. Rev. Lett.* **62** (1989) 2925.
 J.B.J.M. Lanen, R.G. Lovas, A.T. Kruppa, H.P. Blok, J.F.J. van den Brand, R. Ent, E. Jans, G.J. Kramer, L. Lapikás, E.N.M. Quint, G. van der Steenhoven, P.C. Tiemeijer and P.K.A. de Witt Huberts, *Phys. Rev. Lett.* **63** (1989) 2793.
 J.B.J.M. Lanen, H.P. Blok, E. Jans, L. Lepikás, G. van der Steenhoven and P.K.A. de Witt Huberts, *Phys. Rev. Lett.* **64** (1990) 2250.
- [12] T. Tamae, M. Sugawara, K. Yoshida, O. Konno, T. Sasanuma, M. Muto, Y. Shibasaki, T. Tanaka, M. Hirooka, K. Yamada, T. Terasawa, M. Urasawa, T. Ichinohe, S. Takahashi, H. Miyase, Y. Kawazoe, S. Yamamoto and Y. Torizuka, *Nucl. Inst. and Meth.* **A264** (1988) 173.
- [13] T. Tadokoro, T. Hotta, T. Miura, M. Sugawara, A. Takahashi, T. Tamae, E. Tanaka, H. Miyase and H. Tsubota, *Nucl. Phys.* **A575** (1994) 333.
- [14] M. Kimura, Y. Torizuka, K. Shoda, M. Sugawara, T. Saito, M. Oyamada, K. Nakahara, K. Itoh, K. Sugiyama, M. Goto, K. Miyasita and K. Kurahashi, *Nucl. Instr. Meth.* **95** (1971) 403.
- [15] G.C. Li, I. Sick, R.R. Whitney and M.R. Yearian, *Nucl. Phys.* **A162**(1971)583.
- [16] W.E. Kleppinger and J.D. Walecka, *Ann. Phys.* **146** (1983) 349, *Ann. Phys.* **151**(1983)497.
- [17] F. Ajzenberg-Selove, *Nucl. Phys.* **A490** (1988) 1.
- [18] Computer code; DWEOPY, C. Giusti and F.D. Pacati, *Nucl. Phys.* **A473** (1987) 717.
- [19] R.G. Lovas, A.T. Kruppa and J.B.J.M. Lanen, *Nucl. Phys.* **A516** (1990) 325
- [20] T.W. Donnelly and J.D. Walecka, *Phys. Lett.* **B44** (1973) 330.
- [21] B.A. Watson, P.P. Singh and R.E. Segel, *Phys. Rev.* **182** (1969) 977.